Detecting Symmetry Breaking in Magic Angle Graphene Using Scanning Tunneling Microscopy

Jung Pyo Hong, Tomohiro Soejima (□□□□), and Michael P. Zaletel

Phys. Rev. Lett. **129**, 147001 — Published 26 September 2022

DOI: 10.1103/PhysRevLett.129.147001

Detecting symmetry breaking in magic angle graphene using scanning tunneling microscopy

Jung Pyo Hong,[1,*] Tomohiro Soejima (副島智大),[2,*] and Michael P. Zaletel[2,3]
[1]Department of Physics, Princeton University, Princeton, NJ 08540, USA
[2]Department of Physics, University of California, Berkeley, CA 94720, USA
[3]Materials Sciences Division, Lawrence Berkeley National Laboratory, Berkeley, CA 94720, USA
(Dated: August 29, 2022)

A growing body of experimental work suggests that magic angle twisted bilayer graphene exhibits a "cascade" of spontaneous symmetry breaking transitions, sparking interest in the potential relationship between symmetry-breaking and superconductivity. However, it has proven difficult to find experimental probes which can unambiguously identify the nature of the symmetry breaking. Here we show how atomically-resolved scanning tunneling microscopy can be used as a fingerprint of symmetry breaking order. By analyzing the pattern of sublattice polarization and "Kekulé" distortions in small magnetic fields, order parameters for each of the most competitive symmetry-breaking states can be identified. In particular, we show that the "Kramers intervalley coherent state," which theoretical work predicts to be the ground state at even integer fillings, shows a Kekulé distortion which emerges only in a magnetic field.

Since superconductivity and correlated insulators (CIs) were found in magic angle twisted bilayer graphene (MATBG) [1–3], there have been vigorous attempts to identify the nature of the ground states at integer fillings. While widely believed to arise from spontaneous symmetry-breaking in the space of spin and valley, theoretical works have identified a wealth of candidate states which are close in energy, including insulators in the $U(4) \times U(4)$ manifold [4–6], a nematic semi-metal (nSM) [7, 8], and the incommensurate Kekulé spiral (IKS) [9]. However, clear experimental identification of the ground state order has proven difficult.

Scanning tunneling microscopy (STM), which measures the local density of states (LDOS), is a promising tool for distinguishing between these phases. Thus far STM measurements in MATBG have largely focused on modulations in the LDOS at the Moiré-scale [7, 10–13]. STM has found evidence for a "cascade" of putative symmetry breaking transitions [11, 14], but has not yet detected the relevant order parameters. Take, for example, the Kramers-intervalley coherent (K-IVC) state [4, 6, 9, 15] and the nSM [8], which are believed to compete at the charge neutrality point (CNP) [16–18]. While there are quantitative differences between the DOS of the two phases (they are gapped and semimetallic respectively), given finite energy resolution their DOS are in practice very similar (Fig. 1(c)), making discrimination difficult [16]. Furthermore, the Moiré-scale spatial modulation of the LDOS is largely dominated by the peaks at the triangular-lattice of AA-regions [7, 10, 13]. This is a feature of the flat bands common to all the phases, and it is thus inadequate for identifying the ground state. What is needed is a probe capable of directly measuring the order parameter of the symmetry breaking.

In this work we show that atomically-resolved STM measurements are an ideal method for distinguishing between these competing states. By measuring sublattice polarization, bond nematicity, and Kekulé pattern, we can distinguish the following states based on their symmetry properties: 1) symmetric Dirac semimetal 2) nSM 3) K-IVC 4) Generic IVC state (e.g. IKS) 5) valley Hall (VH) and 6) valley polarized (VP) (Table. I, Fig. 1).

The fact that the K-IVC can be distinguished from a generic IVC state may come as a surprise. This is because the "Kramer's time-reversal" symmetry $\mathcal{T}'$ extinguishes any Kekulé charge-density signal. Applying perpendicular magnetic field breaks this symmetry, which reveals the underlying IVC nature of the state.

The ability of atomically-resolved STM to detect symmetry breaking in low-density flat-bands was recently demonstrated experimentally by Liu et al. [19]. They were able to probe the symmetry breaking in the zeroth Landau-level of monolayer graphene by directly measuring sublattice polarization and Kekulé order. As the Landau-levels and MATBG bands have comparable electron densities and energy scales, their findings are encouraging for the analogous measurements in MATBG.

Active bands of twisted bilayer graphene.— We first review the flat band physics of MATBG and set the notation. We focus on a single spin-species case for simplicity. A convenient basis for the four flatbands (per spin) of MATBG is the "Chern" (or chiral) basis $|\mathbf{k}, \tau, C\rangle$, where $\mathbf{k}$ is crystal momentum in the mini-BZ, $\tau = \pm 1$ is the valley label, and $C = \pm 1$ is the Chern number [4, 20]. We can obtain the Chern basis by demanding $\mathcal{C}_2\mathcal{T}$ symmetry to act as $\mathcal{C}_2\mathcal{T}\,|k, \tau, C\rangle = |k, \tau, -C\rangle$. To a good approximation, the Chern basis is sublattice-polarized according to $A/B = \sigma = C\tau$. We further gauge-fix by demanding two-fold rotation $\mathcal{C}_2$ to act as $\mathcal{C}_2\,|k, \tau, C\rangle = |-\mathbf{k}, -\tau, C\rangle$.

Neglecting small Umklapp terms, the Hamiltonian is invariant under valley-dependent phase rotation $U_V(1)$.

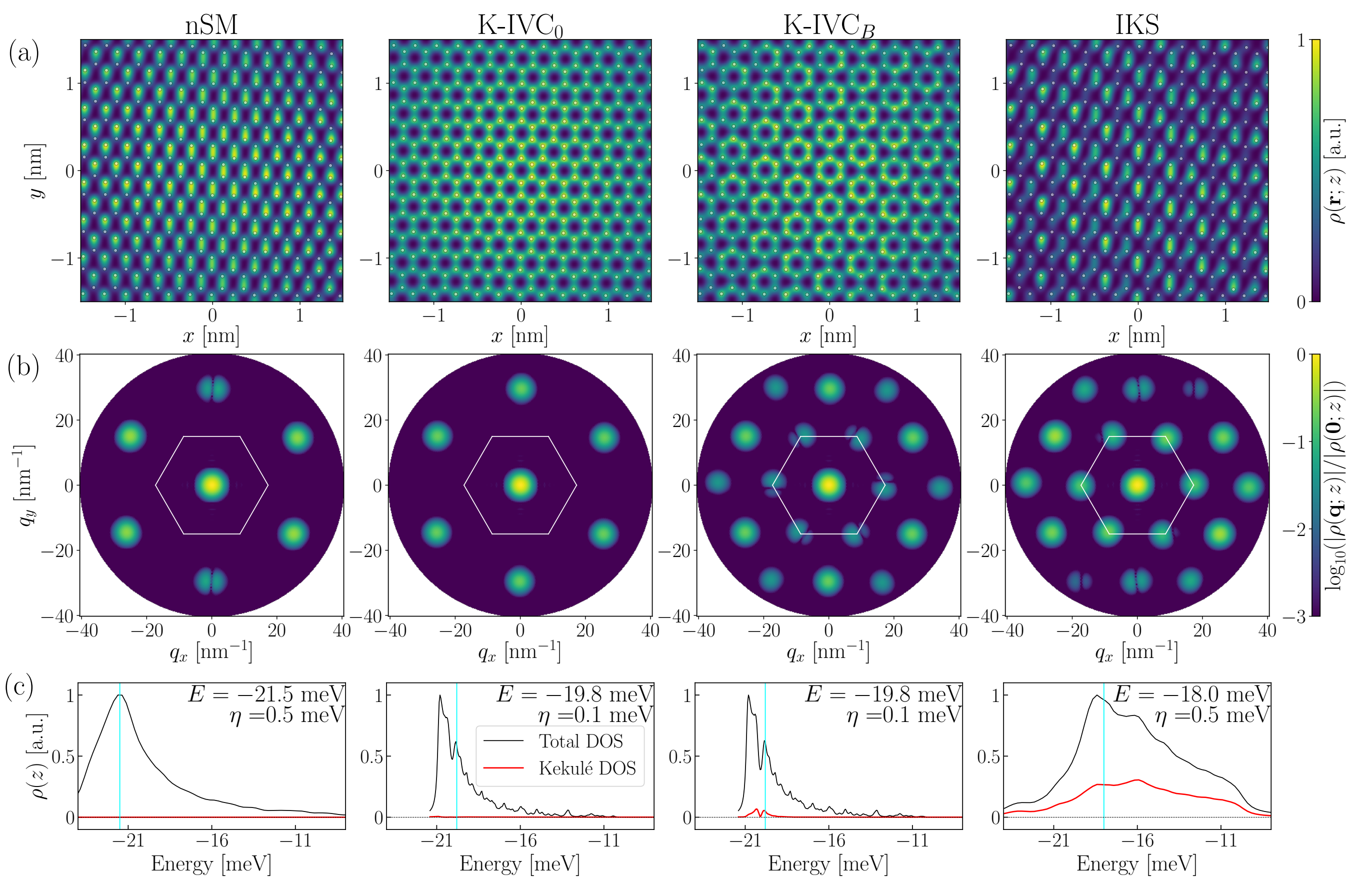

FIG. 1. Spectroscopy calculation results for the self-consistent HF solutions of spinless nSM, K-IVC$_0$, K-IVC$_B$ states at CNP ($\nu = 0$) and IKS states at $\nu = -1$. We present (a) total LDOS $\rho(\mathbf{r}; z)$ (b) total FTLDOS $\rho(\mathbf{q}; z)$ (c) total and Kekulé -DOS $\rho(z = E + i\eta)$ signals for the bottom layer AA-region of MATBG. The signals are normalized by their maximum. For FTLDOS, logarithm is taken on the normalized signals. Cyan lines in (c) indicate the scanning-energy, and the energy range was chosen to show the occupied states. White dots in (a) denote carbon lattice sites.

Using the Pauli matrix notation for τ, the action of $U_V(1)$ is written as $e^{i\tau_z\theta}|\mathbf{k}, \tau, C\rangle = e^{i\tau\theta}|\mathbf{k}, \tau, C\rangle$.

STM-spectroscopy from self-consistent Hartree-Fock calculation.— Let us now review our numerical method. While many of our predictions presented below are based on symmetry considerations, we also numerically computed the LDOS of various competing phases using self-consistent Hartree-Fock (HF) method. We consider an interacting Hamiltonian in which the Coulomb interaction is projected into the flatbands of the Bistritzer-MacDonald (BM) continuum model [21]. Several studies have shown that HF is accurate at even-integer fillings [4, 6, 15, 22–24], in some cases producing ground states nearly identical to the semi-exact solutions obtained from DMRG and exact diagonalization [16, 25–27].

We also incorporate the effect of a perpendicular magnetic field via the phenomenological Hamiltonian $H_{\text{pert}} = E_B C$, where $E_B = 0.1\,\text{meV}$. This choice will be justified in a later section. States under magnetic field are denoted by a subscript B.

We use the single-particle eigenstates $|E_i\rangle$ of the HF effective Hamiltonian H_{eff} to obtain the LDOS:

$$\text{LDOS}(E, \mathbf{r}) = -\frac{1}{\pi}\Im\sum_i \frac{|\langle\mathbf{r}|E_i\rangle|^2}{E_i - E + i\eta}, \tag{1}$$

where E is the scanning-energy of the electron and η is a Lorentzian-broadening parameter [28]. We may similarly obtain the Fourier-transformed LDOS (FTLDOS) $\rho(\mathbf{q}; E)$, and the total DOS $\rho(E)$. We refer to the Supplementary Material (SM) [29] for the full specification of the model, HF calculations, and LDOS/FTLDOS/total DOS calculations.

STM-spectroscopy of competing phases.— Different ground state candidates have different symmetry properties (Table. I), which allow us to distinguish them using STM. The main features are 1) Breaking of $\mathcal{C}_2$ symmetry via sublattice polarization, 2) breaking of $\mathcal{C}_3$ symmetry via bond nematicity, and 3) breaking of graphene-scale translation symmetry via a Kekulé pattern. In order to observe rotational symmetry breaking, we measure the LDOS around $\mathcal{C}_2$ and $\mathcal{C}_3$ symmetry invariant AA-region

Phase	$U_V(1)$	$\mathcal{T}'$	$\mathcal{C}_3$	Kekulé $B=0$	Kekulé $B\neq 0$	S.L. Pol. $B=0$	S.L. Pol. $B\neq 0$
DSM	✓	✓	✓	✗	✗	✗	✗
nSM	✓	✓	✗	✗	✗	✗	✗
VH	✓	✓	✓	✗	✗	✓	✓
VP	✓	✗	✓	✗	✗	✗	✓
K-IVC	✗	✓	✓	✗	✓	✗	✗
IKS	✗	✗	✗	✓	✓	✗	✗

TABLE I. Symmetry properties of various ground state candidate states. DSM stands for symmetric Dirac semimetal. The column for Kekulé denotes absence (✗) or presence (✓) of Kekulé pattern in LDOS. The column for S.L. Pol. indicates whether the LDOS is A/B sublattice polarized at the very center of the AA-stacking region, when averaging over 3 unit cells to remove contributions from the Kekulé signal.

(AB/BA-region can also show interesting features[29]).

To illustrate this point, here we will focus on the following three states that were shown by prior works to be most competitive at even integer fillings of the spinful model: the nSM [8, 25, 26], K-IVC [4, 6, 15, 16], and IKS [9]. These states are predicted to undergo a quantum phase transition to each other under change of heterostrain [9, 16], so it is of great interest to distinguish them using a local probe.

In Fig. 1, we present the total LDOS/FTLDOS/DOS of the bottom layer in the region of AA-stacking for these phases. Let us now walk through the features which are characteristic of each phase.

(i) nSM: Reflecting the nematic nature of the state, the LDOS strongly breaks $\mathcal{C}_3$ but preserves $\mathcal{C}_2$. The order manifests in two forms: first, in the orientation of the strong bonds, and second, while the very center of the AA-region has equal weight on the two sublattices, to the right(left) the dominant weight shifts to the $A(B)$ sublattice. This polarization is not observed along the axis rotated by $2\pi/3$ (Fig. 1 (a)). FTLDOS also show nematicity, where two of the six Bragg peaks (at the reciprocal vectors of the graphene lattice) have a nodal line across which the phase changes over the mini-BZ (Fig. 1 (b)). Similar nematic behavior was observed in earlier STM experiments [13].

(ii-a) K-IVC$_0$: The LDOS respects all the symmetries (Fig. 1 (a)). The absence of a Kekulé pattern despite the inter-valley coherence is enforced by the $\mathcal{T}'$-selection rule to be derived later. The FTLDOS is peaked only at the graphene reciprocal vectors (Fig. 1 (b)).

(ii-b) K-IVC$_B$: For a small range of tunneling bias (Fig. 1 (c)) the LDOS shows a $\sqrt{3}\times\sqrt{3}$ Kekulé pattern respecting $\mathcal{C}_3$. The FTLDOS exhibits dominant peaks at the Bragg points and subdominant peaks at intervalley-scattering momenta $K-K'$ (Fig. 1 (b)). The Kekulé signal only shows up for a range of bias close to the van-Hove peak (see Kekulé -DOS, Fig. 1(c)), and in fact the signal changes sign as the peak is crossed. The origin of this energy dependence will become clear shortly.

(iii) IKS: The LDOS exhibits a $\sqrt{3}\times\sqrt{3}$ bond nematic pattern(Fig. 1 (a)). [30]. The graphene Bragg peaks show similar nodal line as in the nSM (Fig. 1 (b)), reflecting the similarity of IKS to nSM [9]. The Kekulé -DOS is on the same order as the total DOS over the entire range of occupied band energies (Fig. 1 (c)) [31].

The other three phases (DSM, VP, and VH) are discussed in detail in the SM [29].

Vanishing Kekulé signal of the K-IVC state.— We now explain why the K-IVC Kekulé signal emerges only in a magnetic field. We focus on the spinless case for simplicity, and leave the spinful case to the SM [29]. In Ref. [4] it was shown that the K-IVC state produces a Kekulé -like pattern of circulating currents not charge, as shown in Fig. 2(a). This is a consequence of a modified "Kramer's" time-reversal symmetry of K-IVC $\mathcal{T}'=\tau_z\mathcal{T}$ which applies a π-phase rotation between the valleys [4]. We may formalize this extinction as a selection rule on the FTLDOS

$$\rho(\mathbf{q};z=E+i\eta)=\frac{-1}{2\pi i}\left(\mathrm{Tr}[\hat\rho_{\mathbf{q}}\hat G(z)]-\overline{\mathrm{Tr}[\hat\rho_{-\mathbf{q}}\hat G(z)]}\right), \tag{2}$$

where $\hat G(z)$ is the electron Green's function and $\hat\rho_{\mathbf{q}}=e^{-i\mathbf{q}\cdot\hat{\mathbf{r}}}$ is the density operator [29]. The "Kekulé -LDOS" is the portion of the FTLDOS at inter-valley momentum transfer $\mathbf{q}=\pm(K-K')+\Delta\mathbf{q}$, where $\Delta\mathbf{q}$ is small.

We consider either a unitary symmetry with $\mathcal{U}^{-1}\hat G(z)\mathcal{U}=\hat G(z)$ or an anti-unitary symmetry with $\mathcal{K}^{-1}\hat G(z)\mathcal{K}=\hat G^\dagger(z)$. Suppose further that for some $\mathbf{q}$ of interest the density transforms either as $\mathcal{U}^{-1}\hat\rho_{\mathbf{q}}\mathcal{U}=\pm\hat\rho_{\mathbf{q}}$, or $\mathcal{K}^{-1}\hat\rho_{\mathbf{q}}\mathcal{K}=\pm\hat\rho_{-\mathbf{q}}$, where the sign $\pm$ will depend on the symmetry. By inserting these transformations into Eq.(2) [29], we obtain $\rho(\mathbf{q};z)=\pm\rho(\mathbf{q};z)$. The odd case then enforces an extinction.

For the case at hand, we expand the inter-valley part of $\hat\rho_{\mathbf{q}}$ in a plane-wave basis $\langle\mathbf{r}|\mathbf{k},\tau\rangle\propto e^{i(\mathbf{k}+K_\tau)\cdot\mathbf{r}}$

$$\hat\rho_{(\mathbf{q}=K-K'+\Delta\mathbf{q})}=\sum_{\mathbf{k}}|\mathbf{k}+\Delta\mathbf{q},\tau=1\rangle\langle\mathbf{k},\tau=-1|, \tag{3}$$

where $\mathbf{k}$ is restricted to the vicinity of the graphene Dirac points. In the absence of IVC order, the symmetry $\mathcal{U}=\tau_z\in U_V(1)$ gives $\mathcal{U}^{-1}\hat\rho_{\mathbf{q}}\mathcal{U}=-\hat\rho_{\mathbf{q}}$, enforcing an extinction, while for a generic IVC the Kekulé -LDOS will be present. For the K-IVC we instead leverage $\mathcal{T}'|\mathbf{k},\tau\rangle=\tau|-\mathbf{k},-\tau\rangle$, giving $\mathcal{T}'^{-1}\hat\rho_{\mathbf{q}}\mathcal{T}'=-\hat\rho_{-\mathbf{q}}$, and conclude the K-IVC has vanishing Kekulé -LDOS.

Effect of a $\mathcal{T}'$-breaking perturbation.— In the presence of a $\mathcal{T}'$-breaking perturbation H_{pert} - e.g., an applied perpendicular magnetic field B - the selection rule is inoperative and the K-IVC$_B$ phase will generically manifest a Kekulé pattern. In order to understand its magnitude and the sensitive E-dependence found in Fig. 1(c), we now analyze an approximate form of H_{pert} in detail.

An out-of plane B-field will have two effects. First, it

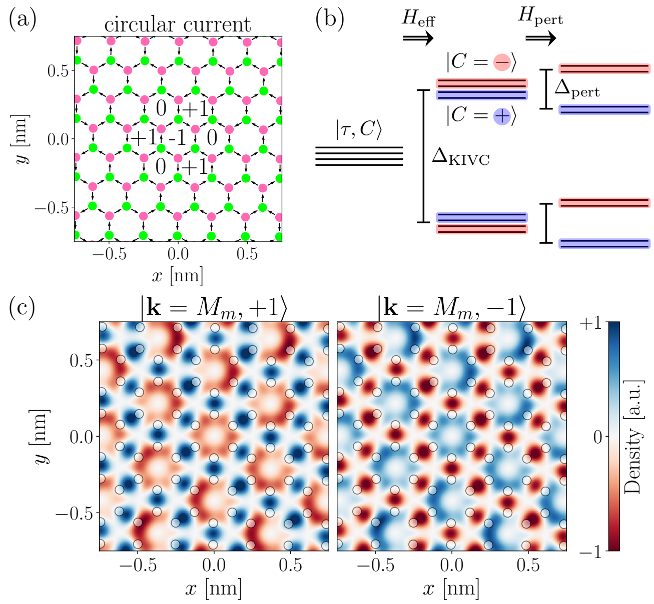

FIG. 2. (a) Total current-density of K-IVC eigenstates (Eq.(5)) $|\mathbf{k}=M_m, n=\pm 1\rangle$. M_m is the M-point of the mini-BZ. Lime/pink dots are the A/B sublattice sites. (b) Schematic representation of the energy levels of K-IVC. From left to right: the basis states; K-IVC eigenstates; perturbation eigenstates (Eq.(4)). Red(blue) corresponds to superposed states with predominantly Chern $+1$ (-1) character. (c) Kekulé charge-density of $|\mathbf{k}=M_m, \mathrm{occ}, n=\pm 1\rangle$.

will reconstruct the flat bands into a Hofstadter butterfly; however this effect is small for weak ($B<1\,\mathrm{T}$) fields [32]. Second, B will couple to the orbital magnetic moment $m(\mathbf{k},\tau,C)=\mu_B g(\mathbf{k},\tau,C)$ of the flat bands, where $g\sim 2-10$ [33–35]. For simplicity we neglect the $\mathbf{k}$-dependence, in which case symmetry enforces the simpler form $m(\mathbf{k},\tau,C)=\mu_B g C$, so that $H_{\rm pert}=E_B C, E_B=\mu_B g B$. For a $B=1\,\mathrm{T}$ field, $E_B\sim 0.1\,\mathrm{meV}$ is thus a conservative estimate of its magnitude.

To compute the change in the LDOS, we diagonalize $H_{\rm eff}+H_{\rm pert}$, as shown schematically in Fig. 2(b). Since $H_{\rm pert}$ is small compared to the gap $\Delta_{\rm KIVC}\sim 20$ meV of $H_{\rm eff}$ (Fig. 3(a)), we project $H_{\rm pert}$ into the space spanned by the two occupied eigenstates $|\mathbf{k}, n=0/1\rangle$ of $H_{\rm eff}$. To constrain the form of $H_{\rm pert}$, we combine $\mathcal{C}_2$, $\mathcal{T}$, and a relative valley phase to obtain a second symmetry of the K-IVC, $\mathcal{C}_2\mathcal{T}''=\mathcal{C}_2\mathcal{T}e^{i\tau_z(\theta_{\rm IVC}-\pi/2)/2}$, which acts locally in $\mathbf{k}$. Because $E_B C$ anti-commutes with $\mathcal{C}_2\mathcal{T}''$, the projection is constrained to take the general form

$$[H_{\rm eff}+H_{\rm pert}](\mathbf{k})=\begin{pmatrix}E_0(\mathbf{k}) & 0\\ 0 & E_1(\mathbf{k})\end{pmatrix}+\begin{pmatrix}0 & \Delta_B(\mathbf{k})\\ \overline{\Delta}_B(\mathbf{k}) & 0\end{pmatrix}. \tag{4}$$

The effect of the perturbation is controlled by the ratio of $\Delta E(\mathbf{k})=E_1(\mathbf{k})-E_0(\mathbf{k})$ and the perturbation $\Delta_B(\mathbf{k})$. In Fig. 3(a,c) we see that $\Delta E(\mathbf{k})$ is much smaller than the band-gap $\Delta_{\rm KIVC}$ across most of the mini-BZ. A small Δ_B could thus result in a significant change in the LDOS even while the ground-state itself changes by a negligible amount of order $H_{\rm pert}/\Delta_{\rm KIVC}\ll 1$.

It is instructive to construct eigenstates of $H_{\rm pert}$ in terms of the valley/Chern basis $|\mathbf{k},\tau,C\rangle$. In the strong-coupling limit, it is given by the following Chern polarized states that span the occupied K-IVC bands[4]:

$$|\mathbf{k},\mathrm{occ},+\rangle \approx (|\mathbf{k},+,+\rangle + e^{i\theta_{\rm IVC}}\,|\mathbf{k},-,+\rangle)/\sqrt{2}, \tag{5}$$

$$|\mathbf{k},\mathrm{occ},-\rangle \approx (|\mathbf{k},+,-\rangle - e^{i\theta_{\rm IVC}}\,|\mathbf{k},-,-\rangle)/\sqrt{2}. \tag{6}$$

Individually, each Chern sector $|\mathbf{k},\mathrm{occ},\pm\rangle$ contributes to Kekulé -LDOS, as shown in Fig. 2(c). However, $\mathcal{T}'$ ensures that the Kekulé contribution from $|\mathbf{k},\mathrm{occ},+\rangle$ and $|-\mathbf{k},\mathrm{occ},-\rangle$ cancel [29]. The perturbation, however, shifts their contributions to the LDOS in energy, and a net signal appears.

K-IVC band-structure.— As an explicit illustration of the $\mathcal{T}'$-breaking mechanism we compute the band-structures of K-IVC$_0$ and K-IVC$_B$. The occupied DOS of KIVC$_0$ (Fig. 3(d)) has a dominant peak at $E_{\rm vH}\sim -20\,\mathrm{meV}$ which is in fact composed of two van-Hove singularities separated by $\Delta E_{\rm vH}\sim 0.5\,\mathrm{meV}$. These two peaks originate from two different bands $|\mathbf{k}, n=0/1\rangle$, so we may estimate $|\Delta E(\mathbf{k})|\sim\Delta E_{\rm vH}$. Indeed, the eigenstates of K-IVC$_B$ shows substantial Chern-polarization (Fig. 3(c)) for $E_B=0.1\,\mathrm{meV}$. When probing the LDOS at energies near the higher (lower) vH peak, we couple predominantly to the $C=1(-1)$ sector, and hence their Kekulé signals (Fig. 2(c)) no longer cancel. The two peaks have opposite Kekulé signal; for the experiment to work, it is thus crucial that the broadening η remains smaller than the peak separation $\sim\Delta E_{\rm vH}$.

Discussion.— There has already been some work on atomically-resolved STM measurement of MATBG. In particular, Ref. [13] found a nematic state at the CNP, and observed a stripe-like signal in the atomically-resolved LDOS of the AB/BA-regions. This feature is consistent with our LDOS calculations for the nSM (see [29] for AB/BA-regions), suggesting they have identified the nSM as the ground state of this sample.

We note that while we have analyzed insulators of MATBG, the symmetry analysis applies more generally. It should thus be possible to map out the symmetry-breaking order as a function of electron density, and correlate it with the observed "cascade". Furthermore, since magic angle twisted trilayer graphene (MATTG) features the same symmetries and band topology [36–38], our conclusions apply to STM measurements [39, 40] of MATTG *mutatis mutandis.*

We thank P. Ledwith, E. Khalaf, D. Parker, and A. Vishwanath for discussions on the role of magnetic fields in producing a K-IVC Kekulé signal. We thank N. Bultinck and S. Chatterjee for our earlier collaborations, and M. Crommie for helpful discussions. MPZ is indebted to

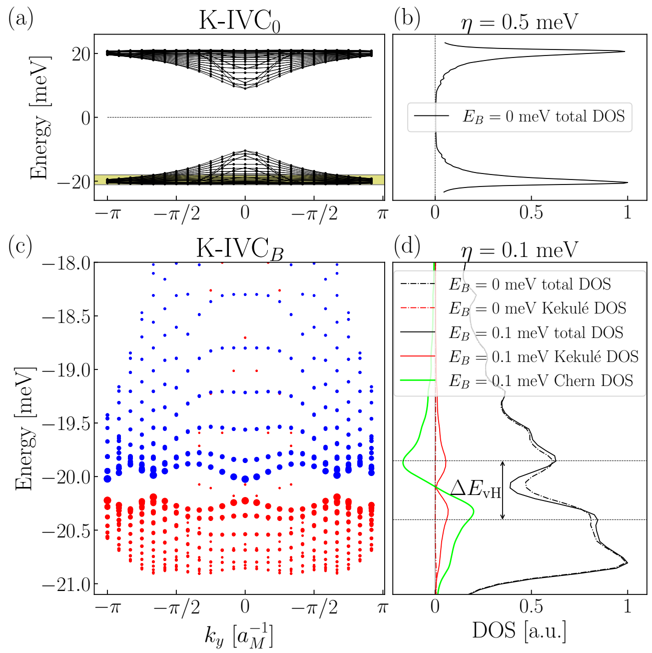

FIG. 3. (a-b) Self-consistent HF band-structure and DOS of K-IVC$_0$ at CNP and $\eta = 0.5\,$meV. Yellow patch denotes the spectrum within valence bands probed at $\eta = 0.1\,$meV in (c-d). (c) Band-structure of K-IVC$_B$ at $E_B = 0.1$ meV. Area of the blue (red) dots corresponds to the degree of positive (negative) Chern polarization of the wavefunction. (d) Total/Kekulé -DOS of K-IVC$_0$ and K-IVC$_B$ along with Chern polarization-weighted total DOS.

X. Liu, G. Farahi, CL Xiu, and A. Yazdani for a related and inspiring collaboration on the zeroth Landau-level of graphene. JPH is supported by Princeton University Department of Physics. JPH acknowledges support from the Samsung Scholarship foundation and UC Berkeley Department of Physics during early stage of the work. TS is funded by the Masason foundation. MZ was supported by the ARO through the MURI program (grant number W911NF-17-1-0323) and the Alfred P Sloan Foundation.

Note added – During the final stage of this work, we became aware of a similar work by Călugăru et al. [41], which also computes the STM signal of various TBG states.

---

* These authors contributed equally

[1] Y. Cao, V. Fatemi, A. Demir, S. Fang, S. L. Tomarken, J. Y. Luo, J. D. Sanchez-Yamagishi, K. Watanabe, T. Taniguchi, E. Kaxiras, R. C. Ashoori, and P. Jarillo-Herrero, Correlated insulator behaviour at half-filling in magic-angle graphene superlattices, Nature **556**, 80 (2018).
[2] Y. Cao, V. Fatemi, S. Fang, K. Watanabe, T. Taniguchi, E. Kaxiras, and P. Jarillo-Herrero, Unconventional superconductivity in magic-angle graphene superlattices, Nature **556**, 43 (2018).
[3] M. Yankowitz, S. Chen, H. Polshyn, Y. Zhang, K. Watanabe, T. Taniguchi, D. Graf, A. F. Young, and C. R. Dean, Tuning superconductivity in twisted bilayer graphene, Science **363**, 1059 (2019).
[4] N. Bultinck, E. Khalaf, S. Liu, S. Chatterjee, A. Vishwanath, and M. P. Zaletel, Ground state and hidden symmetry of magic-angle graphene at even integer filling, Phys. Rev. X **10**, 031034 (2020).
[5] O. Vafek and J. Kang, Renormalization group study of hidden symmetry in twisted bilayer graphene with coulomb interactions, Phys. Rev. Lett. **125**, 257602 (2020).
[6] B. Lian, Z.-D. Song, N. Regnault, D. K. Efetov, A. Yazdani, and B. A. Bernevig, Twisted bilayer graphene. iv. exact insulator ground states and phase diagram, Phys. Rev. B **103**, 205414 (2021).
[7] Y. Choi, J. Kemmer, Y. Peng, A. Thomson, H. Arora, R. Polski, Y. Zhang, H. Ren, J. Alicea, G. Refael, F. von Oppen, K. Watanabe, T. Taniguchi, and S. Nadj-Perge, Electronic correlations in twisted bilayer graphene near the magic angle, Nature Physics **15**, 1174 (2019).
[8] S. Liu, E. Khalaf, J. Y. Lee, and A. Vishwanath, Nematic topological semimetal and insulator in magic-angle bilayer graphene at charge neutrality, Phys. Rev. Research **3**, 013033 (2021).
[9] Y. H. Kwan, G. Wagner, T. Soejima, M. P. Zaletel, S. H. Simon, S. A. Parameswaran, and N. Bultinck, Kekulé spiral order at all nonzero integer fillings in twisted bilayer graphene, Phys. Rev. X **11**, 041063 (2021).
[10] A. Kerelsky, L. J. McGilly, D. M. Kennes, L. Xian, M. Yankowitz, S. Chen, K. Watanabe, T. Taniguchi, J. Hone, C. Dean, A. Rubio, and A. N. Pasupathy, Maximized electron interactions at the magic angle in twisted bilayer graphene, Nature **572**, 95 (2019).
[11] D. Wong, K. P. Nuckolls, M. Oh, B. Lian, Y. Xie, S. Jeon, K. Watanabe, T. Taniguchi, B. A. Bernevig, and A. Yazdani, Cascade of electronic transitions in magic-angle twisted bilayer graphene, Nature **582**, 198 (2020).
[12] Y. Xie, B. Lian, B. Jäck, X. Liu, C.-L. Chiu, K. Watanabe, T. Taniguchi, B. A. Bernevig, and A. Yazdani, Spectroscopic signatures of many-body correlations in magic-angle twisted bilayer graphene, Nature **572**, 101 (2019).
[13] Y. Jiang, X. Lai, K. Watanabe, T. Taniguchi, K. Haule, J. Mao, and E. Y. Andrei, Charge order and broken rotational symmetry in magic-angle twisted bilayer graphene, Nature **573**, 91 (2019).
[14] Y. Choi, H. Kim, Y. Peng, A. Thomson, C. Lewandowski, R. Polski, Y. Zhang, H. S. Arora, K. Watanabe, T. Taniguchi, J. Alicea, and S. Nadj-Perge, Correlation-driven topological phases in magic-angle twisted bilayer graphene, Nature **589**, 536 (2021).
[15] Y. Zhang, K. Jiang, Z. Wang, and F. Zhang, Correlated insulating phases of twisted bilayer graphene at commensurate filling fractions: A Hartree-Fock study, Physical Review B **102**, 035136 (2020).
[16] D. E. Parker, T. Soejima, J. Hauschild, M. P. Zaletel, and N. Bultinck, Strain-Induced Quantum Phase Transitions in Magic-Angle Graphene, Physical Review Letters **127**, 027601 (2021).
[17] J. S. Hofmann, E. Khalaf, A. Vishwanath, E. Berg, and J. Y. Lee, Fermionic monte carlo study of a realistic model of twisted bilayer graphene, Phys. Rev. X **12**, 011061 (2022).

[18] G. Pan, X. Zhang, H. Li, K. Sun, and Z. Y. Meng, Dynamical properties of collective excitations in twisted bilayer graphene, Phys. Rev. B **105**, L121110 (2022).
[19] X. Liu, G. Farahi, C.-L. Chiu, Z. Papic, K. Watanabe, T. Taniguchi, M. P. Zaletel, and A. Yazdani, Visualizing broken symmetry and topological defects in a quantum hall ferromagnet, Science **375**, 321 (2022).
[20] G. Tarnopolsky, A. J. Kruchkov, and A. Vishwanath, Origin of magic angles in twisted bilayer graphene, Phys. Rev. Lett. **122**, 106405 (2019).
[21] R. Bistritzer and A. H. MacDonald, Moiré bands in twisted double-layer graphene, Proceedings of the National Academy of Sciences **108**, 12233 (2011).
[22] M. Xie and A. H. MacDonald, Nature of the Correlated Insulator States in Twisted Bilayer Graphene, Physical Review Letters **124**, 097601 (2020).
[23] J. Liu and X. Dai, Theories for the correlated insulating states and quantum anomalous Hall effect phenomena in twisted bilayer graphene, Physical Review B **103**, 035427 (2021).
[24] T. Cea and F. Guinea, Band structure and insulating states driven by Coulomb interaction in twisted bilayer graphene, Physical Review B **102**, 045107 (2020).
[25] J. Kang and O. Vafek, Non-Abelian Dirac node braiding and near-degeneracy of correlated phases at odd integer filling in magic-angle twisted bilayer graphene, Physical Review B **102**, 035161 (2020).
[26] T. Soejima, D. E. Parker, N. Bultinck, J. Hauschild, and M. P. Zaletel, Efficient simulation of moiré materials using the density matrix renormalization group, Phys. Rev. B **102**, 205111 (2020).
[27] F. Xie, A. Cowsik, Z.-D. Song, B. Lian, B. A. Bernevig, and N. Regnault, Twisted bilayer graphene. VI. An exact diagonalization study at nonzero integer filling, Physical Review B **103**, 205416 (2021).
[28] Note that $V_b = E/e$ is the bias voltage (not measured from the Fermi level, but rather from $E = 0$ determined by our numerical conventions).
[29] See Supplementary Material at [url] for details of Green's function formalism, Hartree-Fock calculations, other numerical data, and additional references [42–47].
[30] IKS (and likewise K-IVC) state enjoys $\mathcal{C}_2\mathcal{T}$ symmetry only when θ_{IVC} takes particular values.
[31] As demonstrated in [29], the Kekulé -DOS signals however vanish for some of the conduction bands due to loss of inter-valley coherence.
[32] At 1 T, the magnetic flux that goes through a Moiré unit cell is about 3% of the flux quantum.
[33] N. Bultinck, S. Chatterjee, and M. P. Zaletel, Mechanism for anomalous hall ferromagnetism in twisted bilayer graphene, Phys. Rev. Lett. **124**, 166601 (2020).
[34] J. Zhu, J.-J. Su, and A. H. MacDonald, Voltage-Controlled Magnetic Reversal in Orbital Chern Insulators, Physical Review Letters **125**, 227702 (2020).
[35] C. L. Tschirhart, M. Serlin, H. Polshyn, A. Shragai, Z. Xia, J. Zhu, Y. Zhang, K. Watanabe, T. Taniguchi, M. E. Huber, and A. F. Young, Imaging orbital ferromagnetism in a moiré Chern insulator, Science **372**, 1323 (2021).
[36] E. Khalaf, A. J. Kruchkov, G. Tarnopolsky, and A. Vishwanath, Magic Angle Hierarchy in Twisted Graphene Multilayers, Physical Review B **100**, 085109 (2019), arXiv:1901.10485.
[37] Y. Cao, J. M. Park, K. Watanabe, T. Taniguchi, and P. Jarillo-Herrero, Pauli-limit violation and re-entrant superconductivity in moiré graphene, Nature **595**, 526 (2021).
[38] Z. Hao, A. M. Zimmerman, P. Ledwith, E. Khalaf, D. H. Najafabadi, K. Watanabe, T. Taniguchi, A. Vishwanath, and P. Kim, Electric field–tunable superconductivity in alternating-twist magic-angle trilayer graphene, Science **371**, 1133 (2021).
[39] S. Turkel, J. Swann, Z. Zhu, M. Christos, K. Watanabe, T. Taniguchi, S. Sachdev, M. S. Scheurer, E. Kaxiras, C. R. Dean, and A. N. Pasupathy, Orderly disorder in magic-angle twisted trilayer graphene, Science **376**, 193 (2022).
[40] H. Kim, Y. Choi, C. Lewandowski, A. Thomson, Y. Zhang, R. Polski, K. Watanabe, T. Taniguchi, J. Alicea, and S. Nadj-Perge, Spectroscopic Signatures of Strong Correlations and Unconventional Superconductivity in Twisted Trilayer Graphene, arXiv:2109.12127 [cond-mat] (2021), arXiv:2109.12127 [cond-mat].
[41] D. Călugăru, N. Regnault, M. Oh, K. P. Nuckolls, D. Wong, R. L. Lee, A. Yazdani, O. Vafek, and B. A. Bernevig, Spectroscopy of Twisted Bilayer Graphene Correlated Insulators, arXiv:2110.15300 [cond-mat] (2021), arXiv:2110.15300 [cond-mat].
[42] A. Thomson, I. M. Sorensen, S. Nadj-Perge, and J. Alicea, Gate-defined wires in twisted bilayer graphene: From electrical detection of intervalley coherence to internally engineered majorana modes, Phys. Rev. B **105**, L081405 (2022).
[43] G. Rickayzen, Green's Functions and Condensed Matter, Materials Science Series (Academic Press, 1980).
[44] A. V. Oppenheim, R. W. Schafer, J. R. Buck, and L. Lee, Discrete-time Signal Processing, Prentice Hall international editions (Prentice Hall, 1999).
[45] Z. Bi, N. F. Q. Yuan, and L. Fu, Designing flat bands by strain, Physical Review B **100**, 035448 (2019).
[46] E. Khalaf, S. Chatterjee, N. Bultinck, M. P. Zaletel, and A. Vishwanath, Charged skyrmions and topological origin of superconductivity in magic-angle graphene, Science Advances **7**, eabf5299 (2021).
[47] S. Chatterjee, N. Bultinck, and M. P. Zaletel, Symmetry breaking and skyrmionic transport in twisted bilayer graphene, Physical Review B **101**, 165141 (2020).